

UC Berkeley

UC Berkeley Previously Published Works

Title

Making ultrastrong steel tough by grain-boundary delamination

Permalink

<https://escholarship.org/uc/item/4cw7c33g>

Journal

Science, 368(6497)

ISSN

0036-8075

Authors

Liu, L
Yu, Qin
Wang, Z
et al.

Publication Date

2020-06-19

DOI

10.1126/science.aba9413

Peer reviewed

Making Ultrastrong Steel Tough by Grain-Boundary Delamination

L. Liu^{1,†}, Qin Yu^{2,†}, Z. Wang¹, Jon Ell^{2,3}, M. X. Huang^{1,*}, Robert O. Ritchie^{2,3*}

¹Department of Mechanical Engineering, The University of Hong Kong, Pokfulam Road, Hong Kong, China.

²Materials Sciences Division, Lawrence Berkeley National Laboratory, Berkeley, CA 94720, USA.

³Department of Materials Science & Engineering, University of California, Berkeley, CA 94720, USA.

†These authors contributed equally to this work.

*Corresponding authors: mxhuang@hku.hk (M.X.H.); roritchie@lbl.gov (R.O.R.)

Abstract: Developing ultrahigh strength steels that are ductile, fracture resistant, and cost-effective would be attractive for a variety of structural applications. We show that improved fracture resistance in a steel with an ultrahigh yield strength of nearly 2GPa can be achieved by activating delamination toughening coupled with transformation induced plasticity. Delamination toughening associated with intensive but controlled cracking at Mn-enriched prior-austenite grain boundaries normal to the primary fracture surface dramatically improves the overall fracture resistance. As a result, fracture under plane-strain conditions is automatically transformed into a series of fracture processes in “parallel” plane-stress conditions through the thickness. The present “high-strength induced multi-delamination” strategy offers a different pathway to develop engineering materials with ultra-high strength and superior toughness at economical materials cost.

One Sentence Summary: Delamination (crack-divider) toughening allows development of a super-tough, high yield strength steel at low cost.

Lightweight yet cost-efficient structural materials with superior mechanical properties are continually sought after in engineering applications to meet the demands of sustainable economy development. Unfortunately, attaining high strength is usually at the expense of deteriorating toughness, which invariably is a major concern for safety-critical applications (1, 2). The strengthening mechanisms in structural metals and alloys are built on the fundamental principle of inhibiting, or blocking, dislocation slip by introducing various obstacles at different length-scales (3, 4). However, abundant dislocations entangled in small imperfections can give rise to the localized stress concentrations that can cause crack initiation which eventually can lead to catastrophic failure (1, 5). A mainstream effort to overcome the strength-toughness trade-off is focused on tailoring the microstructure or designing materials by solid-solution alloying. Multi-element high and medium-entropy alloys possess exceptional damage tolerance at cryogenic temperatures because of a deformation-induced nano-twinning mechanism (6, 7). Maraging steels are another example as they are recognized as the strongest metal alloys with acceptable damage tolerance for aerospace applications. However, maraging steels contain a large amount

of costly alloying elements like nickel (17-19 wt.%), cobalt (8-12 wt.%) and molybdenum (3-5 wt.%) (8). Although the maraging steel alloying strategy is a perfect vehicle to attain superior mechanical performance, economical mass production and recycling are not feasible due to costs and environmental concerns (3, 9). Reducing the average grain size is a different non-alloying pathway to enhance the strength-toughness combination. However, this approach can be limiting because the strengthening is usually achieved at the sacrifice of losing ductility (10, 11). We show here that exceptional damage-tolerance can be achieved in an ultrastrong steel, with a simple composition and cost-effective processing route for fabrication. We demonstrate that increasing the yield strength is not detrimental to the toughness, but instead it can facilitate the activation of a delamination toughening (12, 13) mechanism. This substantially enhances the toughness. Specifically, the ultrahigh yield strength enables a secondary fracture mode, delamination cracking, at interfaces normal to the primary fracture surface. Multiple separated laminated ligaments develop near the fracture surface because of the delamination events, providing an extra energy release rate for fracture as well as enhancing crack-tip blunting, collectively elevating the overall fracture toughness. Such delamination toughening combined with transformation-induced plasticity (TRIP) toughening are rarely realized simultaneously in structural materials. The combination enables an intriguing combination of strength, ductility and toughness properties in our steel.

Our steel has a chemical composition of Fe-9.95%Mn-0.44%C-1.87%Al-0.67%V (weight percent) and was fabricated by a deformed and partitioned treatment (14) (Fig. S1). Starting with an almost fully austenitic microstructure (Fig. S2), the prior-austenite grains are extensively elongated along the rolling direction (RD) during the initial hot rolling and warm rolling processes (14, 15). The austenite partially transforms to martensite during the subsequent cold rolling, resulting in a lamellar martensite/austenite duplex microstructure (Fig. 1A), which contains a volume fraction of austenite, measured at 47.5% by neutron diffraction (Fig. S3). Partitioning is finally performed to optimize the mechanical stability of retained austenite by C partitioning from martensite to austenite (Fig. S4) (14). The martensitic matrix (α') is composed of nano-sized grains decorated by intensive dislocations (Fig. S5). The dislocation density of martensite matrix was determined by neutron diffraction to be $2.43 \times 10^{16} \text{ m}^{-2}$ which is at least one order higher than that of other martensitic steels (Fig. S6); further details of this calculation based on neutron diffraction measurements are given in ref. (16). The austenite (γ) phase displays a stretched lamellar-shaped grain structure with dimensions of hundreds of micrometers along the RD, dozens of micrometers in the transverse direction (TD), and a few micrometers in the normal direction (ND) (Fig. 1A). Of particular note is that the prior-austenite grain boundaries (PAGBs) are retained during cold rolling where some austenite grains transform to martensite; this is indicated by the black dotted lines in the three-dimensional (3-D) stereographic microstructure in Fig. 1B, reconstructed from the PAGBs maps. Further atomic-scale composition analysis of the present steel by 3-D atom probe topography (APT) shows segregation of Mn and C to the PAGB (Fig. 1C, detailed explanation in (16)). No segregation of P, S and other harmful elements to the PAGB was detected. To better illustrate the laminated duplex microstructure, we constructed a schematic 3-D model (Fig. 1D).

To evaluate the mechanical properties of the ultrastrong steel, we characterized the tensile properties and the J -integral based crack-resistance (J - Δa) R-curves in both the RD and TD orientations in ambient air. The RD (or TD) dog-bone shaped tensile specimen was strained

along (or perpendicular to) the elongated austenitic grains (Fig. 2A). Correspondingly, the notch and crack propagation direction in the RD (or TD) compact-tension C(T) fracture toughness specimens were aligned perpendicular to (or parallel to) the elongated austenitic grains. Benefiting from the unusually high dislocation density, tensile loading along the RD yields a superior combination of strength and ductility (Fig. 2B) (14). Specifically, the upper yield strength (σ_{yu}), the ultimate tensile strength (σ_{uts}) and the uniform elongation (ϵ_u) were determined to be 1,978 MPa, 2,144 MPa and 19.0%, respectively (Fig. 2B and Table S1). Properties in the loading direction along the TD are also sound with a very high ultimate tensile strength of 2,048 MPa similar to that for the RD orientation, but plastic deformation begins to proceed earlier; the 0.2%-offset yield strength (σ_y) in the TD orientation was measured to be 1,714 MPa.

In view of its ultrahigh strength and plastic deformation capacity, we evaluated the fracture resistance of the present steel by measuring J -integral based R-curves, *i.e.*, J as a function of the stable crack extension, Δa , using the C(T) specimens in accordance with the ASTM Standard E1820 (17). Our steel displays a modest fracture toughness when loaded along TD, presenting an average J_{Ic} of 19.6 kJ·m⁻² at crack initiation (Fig. 2C, Table S1). The crack-resistance (R-curve) behavior in the TD slightly rises as the crack extends, resulting in a valid crack-growth toughness of $J_{ss} = 28.7$ kJ·m⁻² at a crack extension Δa of ~1 mm. These fracture properties are comparable to those of the best strong-yet-tough materials, such as 18Ni 300-grade maraging steels (18, 19) and commercial-aircraft-quality 300M and 4340 steels (20, 21). In spite of a higher yield strength of the RD tensile specimens, the R-curve in the RD orientation reveals an even better crack resistance, showing a crack-initiation toughness J_{Ic} of 46.9 kJ·m⁻² and a crack-growth toughness J_{ss} of 84.6 kJ·m⁻² as the crack extends to $\Delta a \sim 1$ mm (Fig. 2C and Table S1). These toughness values in the RD are almost 1.5 and 2 times higher than those in the TD, respectively. According to the standard mode-I J - K equivalence relationship, the crack-initiation toughness, $K_{J_{Ic}}$ of the RD and TD specimens were determined to be 101.5 and 65.4 MPa·m^{1/2}, respectively. Likewise, the crack-growth toughness at $\Delta a \sim 1$ mm, $K_{J_{ss}}$, was 136.4 and 79.4 MPa·m^{1/2} for the RD and TD specimens, respectively. These are very high values of the crack-initiation and crack-growth toughnesses in our ultrastrong steel that are not found in any other existing structural materials at a comparable yield strength (~2 GPa).

To illuminate the underlying toughening mechanisms responsible for the exceptional damage tolerance of the ultrastrong steel, we characterized the microstructures on various sections of the RD and TD C(T) specimens (Figs. 3A and 3E). Featured regions on the fracture surfaces characterized by scanning electron microscopy (SEM) show the existence of multiple thin-layer delamination bands in both RD and TD orientations (Figs. 3B and 3F). Observed from the fracture surface, the original ~1.4 mm-thick RD specimens were delaminated through the thickness into several thin layers with their inter-spacings (or delamination cracks) “penetrating” into the material along the planes perpendicular to the fracture surface. Moreover, delamination cracks at different length-scales were developed in the present steel, resulting in numerous delamination bands sized in the range of several micrometers (Region A in Fig. 3B). The thickness of these delamination ligaments was remarkable thinner than that in other structural materials containing delamination cracks (12, 13). Delamination was also present in the TD specimens, but the delamination cracks were fewer in number and shorter in length than those in the RD specimens. The microstructure in the vicinity of the delamination cracks in the through-thickness sections normal to the fracture surface was further characterized to clarify the micro-

mechanisms associated with the delamination cracks (Figs. 3C and 3G). Based on the statistical distribution of the crack lengths (shown in Figs. S7 and S8), the delamination cracks in the RD specimens can be categorized into two groups: short cracks with lengths $< \sim 50 \mu\text{m}$ (blue arrows in Fig. 3C) and longer cracks with lengths $> \sim 50 \mu\text{m}$ (dark red arrows in Fig. 3C). Moreover, slender cracks disconnected from the fracture surface (pink arrows in Fig. 3C) were usually observed in the vicinity of the long delamination cracks. Further characterization at the tips of the delamination cracks clearly indicated that these cracks propagate predominantly along the PAGBs (Fig. 3C). In the case of the TD specimens, only short delamination cracks with lengths shorter than $50 \mu\text{m}$ were observed (Fig. 3G). Clearly, loading along the RD results in a much larger tendency for delamination.

The activation of delamination toughening requires two necessary conditions: intrinsically and microstructurally, the existence of “relatively weak interfaces”, where delamination takes place; mechanically, with a “high mechanical stress” that exceeds the critical fracture stress of the “relatively weak interfaces”. From our characterization of the locations at delamination crack tips, the Mn-enriched PAGBs in our steel serve as the “relatively weak interfaces” and preferential sites for the initiation and propagation of the delamination microcracks (Figs. 3C and 3G). Actually, the Mn-enriched PAGBs have a high level of cohesion strength, but they are just not as strong as the grain interior due to the segregation of Mn (Fig. 1C) (22, 23). By comparison, such delaminations do not occur in maraging steels, no matter how high their yield strengths are, as there are no such interfaces and preferential sites along the boundaries with reduced cohesion.

From the perspective of the mechanical driving force, a triaxial tensile stress state exists ahead of a crack tip under plane-strain conditions. The material in front of the crack tip is subjected to a tensile stress (σ_2 in Fig. S9A) along the thickness direction (ND in Fig. 1A). When the tensile stress σ_2 that is perpendicular to the PAGBs is sufficiently high to reach the critical fracture stress of the Mn-enriched PAGBs (Fig. 3A), delamination will occur. To meet this requirement, the material should have sufficiently high yield strength so that a high external applied stress is required. A higher external applied stress will lead to a higher σ_2 at the crack tip. For certain structural materials containing weak interfaces, delamination cracks are mainly formed at low temperatures where the interfaces may be more brittle and the through-thickness stresses are larger. This leads to the fascinating effect that such alloys, *e.g.*, certain Al-Li alloys (12) and ultrafine-grained low alloy steels (24, 25), become tougher at cryogenic temperatures compared to ambient temperature. As demonstrated here, the present steel possesses ultrahigh yield strength due to its high dislocation density, and Mn-enriched PAGBs with relatively low cohesion as compared to the grain interior, acting as the preferential delamination sites; this meets the two necessary requirements to activate delamination toughening and leads to its exceptional room-temperature fracture toughness for a metallic alloy with a yield strength in the 2 GPa range.

As a consequence of the multiple delamination cracks occurring ahead of the crack front and perpendicular to the crack plane, the expected fracture under plane-strain conditions is transformed into a series of fracture processes in “parallel” plane-stress ligaments through the thickness which individually display a far higher (plane-stress) toughness than for a single (full-thickness) plane-strain section (Fig. S9B). In parallel, numerous new interfaces generated during

the delamination process consume energy, which effectively increases the energy release rate to contribute to the exceptional fracture toughness. Our current study further reveals that the delamination toughening is affected by the relative orientations of the delamination crack path with respect to the elongated duplex structure. The length of the PAGBs along RD are almost three times of that parallel to TD due to the large rolling reduction (Fig. 1B). As the delamination cracks propagate along the elongated PAGBs parallel to RD in the RD specimens, longer delamination cracks are developed (Fig. 3C). However, delamination cracks extend with short PAGBs parallel to the TD on the through-thickness section in the TD specimen. Furthermore, numerous PAGBs, aligned perpendicular to the crack path, are developed in the TD specimen. These grain boundaries are effective obstacles to retard the propagation of delamination cracks (Fig. 3G). Therefore, the longer (or shorter) delamination cracks developed in the RD (or TD) specimens give rise to a larger (or smaller) toughening effect, which is consistent with the higher (or lower) values of the measured toughness in these orientations.

The present steel also displays a TRIP effect during crack advance. The TRIP-toughening is due to an *in situ* austenite-to-martensite transformation that is triggered in the vicinity of the crack tip, where an initial duplex martensitic/austenitic microstructure (Fig. 1A) is transformed to an almost fully martensitic microstructure (Figs. 3D and 3H) after crack propagation. Due to the lattice-parameter difference between martensite and parent austenite, a compressive residual stress is likely introduced by the TRIP effect in the vicinity of crack tip to further resist crack propagation (26). In addition, TRIP effect can serve to promote strain hardening which, in turn, enhances the uniform ductility by delaying the onset of the necking instability to provide additional intrinsic toughening to resist crack propagation (27, 28).

Similar to the delamination toughening, the TRIP-toughening is also a function of the crack extension orientations. A larger-sized TRIP zone is realized in the RD specimen (Fig. 3D) where the main crack propagates perpendicular to the elongated austenite. In contrast, a small-sized TRIP-zone is produced (Fig. 3H) in the TD specimen because the growth of the TRIP-zone is significantly restricted by the PAGBs parallel to the elongated austenite lamellae (28). This is illustrated in the schematic figures in Figs. 3D and 3H. Consistently, higher (or lower) toughness values exhibited in the RD (or TD) specimens are ascribed to the stronger (or weaker) TRIP toughening effect induced by the larger (or smaller)-sized TRIP zone.

To demonstrate how the excellent damage-tolerance in our steel compares to other ultrahigh strength structural materials, we show in Fig. 4 an Ashby map of the crack-initiation fracture toughness vs. yield strength. Our steel exhibits a comparable yield strength to some of the strongest existing metallic materials, namely maraging steels, but with an initiation toughness (K_{IC}) that is almost a factor of two higher. Indeed, our steel displays a toughness comparable to titanium alloys but with a factor of two higher strength. The exceptional combination of strength and toughness clearly demonstrates that the “high-strength induced multi-delamination” mechanism can be highly effective in maximizing the mechanical properties of high-strength structural materials while minimizing material cost. Our material design principle that exploits high strength combined with relatively weak interfaces, is one that we believe can be widely applied to optimize the mechanical performance of materials with ultrahigh strength.

References and Notes

1. R. O. Ritchie, The conflicts between strength and toughness. *Nature Mater.* **10**, 817 (2011).
2. K. Lu, The future of metals. *Science* **328**, 319-320 (2010).
- 5 3. X. Li, K. Lu, Playing with defects in metals. *Nature materials* **16**, 700 (2017).
4. K. Lu, L. Lu, S. Suresh, Strengthening materials by engineering coherent internal boundaries at the nanoscale. *Science* **324**, 349-352 (2009).
5. M. JW, Z. Guo, K. CR, Y.-H. Kim, The limits of strength and toughness in steel. *ISIJ Int.* **41**, 599-611 (2001).
- 10 6. B. Gludovatz *et al.*, A fracture-resistant high-entropy alloy for cryogenic applications. *Science* **345**, 1153-1158 (2014).
7. B. Gludovatz *et al.*, Exceptional damage-tolerance of a medium-entropy alloy CrCoNi at cryogenic temperatures. *Nature Communications* **7**, 10602 (2016).
8. S. Floreen, The physical metallurgy of maraging steels. *Metall. Reviews* **13**, 115-128 (1968).
- 15 9. X. Li, K. Lu, Improving sustainability with simpler alloys. *Science* **364**, 733-734 (2019).
10. K. Lu, Making strong nanomaterials ductile with gradients. *Science* **345**, 1455-1456 (2014).
11. Y. Wang, M. Chen, F. Zhou, E. Ma, High tensile ductility in a nanostructured metal. *Nature* **419**, 912 (2002).
- 20 12. K. V. Rao, W. Yu, R. Ritchie, Cryogenic toughness of commercial aluminum-lithium alloys: Role of delamination toughening. *Metall. Trans. A* **20**, 485-497 (1989).
13. K. S. Chan, Evidence of a thin sheet toughening mechanism in Al– Fe– X alloys. *Metall. Trans. A* **20**, 155-164 (1989).
- 25 14. B. B. He, B. Hu, H. W. Yen, G. J. Cheng, Z. K. Wang, H. W. Luo, M. X. Huang, High dislocation density–induced large ductility in deformed and partitioned steels. *Science* **357**, 1029-1032 (2017).
15. L. Liu, B.B. He, M.X. Huang, Processing–Microstructure Relation of Deformed and Partitioned (D&P) Steels. *Metals* **9**, 695 (2019).
- 30 16. Materials and methods are available as Supplementary Materials on Science online.
17. E1820-17a Standard Test Method for Measurement of Fracture Toughness, *ASTM Intl.* (2017).
18. C. Carter, Stress corrosion crack branching in high-strength steels. *Eng. Fract. Mech.* **3**, 1-13 (1971).
- 35 19. Y. He, K. Yang, W. Qu, F. Kong, G. Su, Strengthening and toughening of a 2800-MPa grade maraging steel. *Mater. Lett.* **56**, 763-769 (2002).
20. R. O. Ritchie, Influence of microstructure on near-threshold fatigue-crack propagation in ultra-high strength steel. *Metal Sci.* **11**, 368-381 (1977).
21. R. O. Ritchie, B. Francis, W. L. Server, Evaluation of toughness in AISI 4340 alloy steel austenitized at low and high temperatures. *Metall. Trans. A* **7**, 831-838 (1976).
- 40 22. M. Kuzmina, D. Ponge, D. Raabe, Grain boundary segregation engineering and austenite reversion turn embrittlement into toughness: example of a 9 wt.% medium Mn steel. *Acta Mater.* **86**, 182-192 (2015).

23. N. Heo, J. Nam, Y.-U. Heo, S.-J. Kim, Grain boundary embrittlement by Mn and eutectoid reaction in binary Fe–12Mn steel. *Acta Mater.* **61**, 4022-4034 (2013).
22. M. Kuzmina, D. Ponge, D. Raabe, Grain boundary segregation engineering and austenite reversion turn embrittlement into toughness: example of a 9 wt.% medium Mn steel. *Acta Mater.* **86**, 182-192 (2015).
- 5 23. N. Heo, J. Nam, Y.-U. Heo, S.-J. Kim, Grain boundary embrittlement by Mn and eutectoid reaction in binary Fe–12Mn steel. *Acta Mater.* **61**, 4022-4034 (2013).
24. Y. Kimura, T. Inoue, F. Yin, K. Tsuzaki, Inverse temperature dependence of toughness in an ultrafine grain-structure steel. *Science* **320**, 1057-1060 (2008).
- 10 25. J. W. Morris, Stronger, tougher steels. *Science* **320**, 1022-1023 (2008).
26. W. Bleck, X. Guo, Y. Ma, The TRIP effect and its application in cold formable sheet steels. *Steel Research Intl.* **88**, 1700218 (2017).
27. R. H. Leal, Transformation toughening of metastable austenitic steels. Ph.D. Thesis, Massachusetts Institute of Technology, (1984).
- 15 28. M. M. Wang, C. C. Tasan, D. Ponge, A. C. Dippel, D. Raabe, Nanolaminate transformation-induced plasticity–twinning-induced plasticity steel with dynamic strain partitioning and enhanced damage resistance. *Acta Mater.* **85**, 216-228 (2015).
29. M. Linaza, J. Romero, J. Rodriguez-Ibabe, J. Urcola, Improvement of fracture toughness of forging steels microalloyed with titanium by accelerated cooling after hot working. *Scripta Metall. Mater.* **29**, 1217-1222 (1993).
- 20 30. M. E. Haque, K. Sudhakar, ANN back-propagation prediction model for fracture toughness in microalloy steel. *Int. J. Fatigue* **24**, 1003-1010 (2002).
31. S. K. Putatunda, Fracture toughness of a high carbon and high silicon steel. *Mater. Sci. Engin. A* **297**, 31-43 (2001).
- 25 32. J. Kobayashi, D. Ina, A. Futamura, K.-i. Sugimoto, Fracture toughness of an advanced ultrahigh-strength TRIP-aided steel. *ISIJ Int.* **54**, 955-962 (2014).
33. A. Bayram, A. Uğuz, M. Ula, Effects of microstructure and notches on the mechanical properties of dual-phase steels. *Mater. Charact.* **43**, 259-269 (1999).
34. L. Xiong, Z. You, S. Qu, L. Lu, Fracture behavior of heterogeneous nanostructured 316L austenitic stainless steel with nanotwin bundles. *Acta Mater.* **150**, 130-138 (2018).
- 30 35. J. E. Pawel *et al.*, Fracture toughness of candidate materials for ITER first wall, blanket, and shield structures. *J. Nucl. Mater.* **212**, 442-447 (1994).
36. L. Van Swam, R. Pelloux, N. Grant, Properties of maraging steel 300 produced by powder metallurgy. *Powder Metall.* **17**, 33-45 (1974).
- 35 37. R. O. Ritchie, Near-threshold fatigue crack propagation in ultra-high strength steel: influence of load ratio and cyclic strength. *J. Eng. Mater. Technol.* **99**, 195-249 (1977).
38. G. Lai, W. Wood, R. Clark, V. Zackay, E. R. Parker, The effect of austenitizing temperature on the microstructure and mechanical properties of as-quenched 4340 steel. *Metall. Trans.* **5**, 1663-1670 (1974).
- 40 39. H. Aglan, Z. Liu, M. Hassan, M. Fateh, Mechanical and fracture behavior of bainitic rail steel. *J. Mater. Process. Technol.* **151**, 268-274 (2004).
40. C. Garcia-Mateo, F. Caballero, Ultra-high-strength bainitic steels. *ISIJ Intl.* **45**, 1736-1740 (2005).
41. M. D. Demetriou *et al.*, A damage-tolerant glass. *Nature materials* **10**, 123 (2011).

42. N. Kamp, I. Sinclair, M. Starink, Toughness-strength relations in the overaged 7449 Al-based alloy. *Metall. Mater. Trans. A* **33**, 1125-1136 (2002).
43. M. Niinomi, Mechanical properties of biomedical titanium alloys. *Mater. Sci. Engin. A* **243**, 231-236 (1998).
- 5 44. R. Mirshams, C. Xiao, S. Whang, W. Yin, R-curve characterization of the fracture toughness of nanocrystalline nickel thin sheets. *Mater. Sci. Engin. A* **315**, 21-27 (2001).
45. A. Singh, L. Tang, M. Dao, L. Lu, S. Suresh, Fracture toughness and fatigue crack growth characteristics of nanotwinned copper. *Acta Mater.* **59**, 2437-2446 (2011).
46. L. Liu, B. B He, M. X. Huang, Engineering heterogeneous multiphase microstructure by austenite reverted transformation coupled with ferrite transformation. *JOM* **71**, 1322-1328 (2019).
- 10 47. H. Bhadeshia, R. Honeycombe, *Steels: Microstructure and Properties*. Butterworth-Heinemann, 2017.
48. P. J. Withers, Depth capabilities of neutron and synchrotron diffraction strain measurement instruments. I. The maximum feasible path length. *J. Appl. Crystallogr.* **37**, 596-606 (2004).
- 15 49. B. H. Toby, R. B. Von Dreele, GSAS-II: the genesis of a modern open-source all purpose crystallography software package. *J. Appl. Crystallogr.*, **46**, 544-549 (2013).
50. M. Wang, M. Huang, Abnormal TRIP effect on the work hardening behavior of a quenching and partitioning steel at high strain rate. *Acta Mater.*, **188**, 551-559 (2020).
- 20 51. T. Ungár, J. Gubicza, G. Ribárik, A. Borbély, Crystallite size distribution and dislocation structure determined by diffraction profile analysis: principles and practical application to cubic and hexagonal crystals. *J. Appl. Crystallogr.* **34**, 298-310 (2001).
52. T. Ungár, I. Dragomir, Á. Révész, A. Borbély, The contrast factors of dislocations in cubic crystals: the dislocation model of strain anisotropy in practice. *J. Appl. Crystallogr.* **32**, 992-1002 (1999).
- 25 53. T. Ungár, I. Groma, M. Wilkens, Asymmetric X-ray line broadening of plastically deformed crystals. II. Evaluation procedure and application to [001]-Cu crystals. *J. Appl. Crystallogr.* **22**, 26-34 (1989).
- 30 54. A. Devaraj *et al.*, Three-dimensional nanoscale characterisation of materials by atom probe tomography. *Int. Mater. Rev.* **63**, 68-101 (2018).

Acknowledgments

35 L.H. He and J. Chen are acknowledged for their help on the neutron powder diffraction experiments which were performed at GPPD of the China Spallation Neutron Source (CSNS), Dongguan, China. J.H. Luan and Z.B. Jiao are acknowledged for their help on the APT experiments conducted at the Inter-University 3D Atom Probe Tomography Unit of City University of Hong Kong. We thank B.B. He for his assistance with the preparation of the material, and M. Wang for help with the determination of the dislocation density. Finally, we

40 thank Prof. K. Lu for his insightful comments on the paper. **Funding:** M.X.H. acknowledges the financial support from the National Key Research and Development Program of China (No. 2019YFA0209900, 2017YFB0304401), National Natural Science Foundation of China (No. U1764252) and Research Grants Council of Hong Kong (No. R7066-18, 17255016, 17210418). Q.Y. and R.O.R. acknowledge financial support to the Mechanical Behavior of Materials

Program (KC13) at the Lawrence Berkeley National Laboratory (LBNL) provided by the U.S. Department of Energy, Office of Science, Basic Energy Sciences, Materials Sciences and Engineering Division under contract no. DE-AC02-05-CH11231. EBSD experiments were carried out at LBNL's Molecular Foundry supported by the Office of Science, Office of Basic Energy Sciences, of the U.S. Department of Energy under the same contract number. **Author contributions:** M.X.H., Q.Y., and R.O.R designed the research. M.X.H. and R.O.R. supervised the study. L.L. fabricated the steel material. Q.Y., J.E. and L.L. performed the mechanical characterization. L.L., Q.Y. and Z.W. conducted the SEM and EBSD characterizations. L.L. worked on the TEM characterization. L.L. and Z.W conducted the APT measurement and the neutron diffraction characterization. L.L., Q.Y., M.X.H. and R.O.R. analyzed the data and wrote the manuscript. All the authors discussed the results and commented on the manuscript. **Competing interests:** The authors declare no competing interests. **Data and materials availability:** Data are available in the manuscript and supplementary materials.

Supplementary Materials

Materials and Methods

Supplementary Text

Figs. S1 to S9; Tables S1 to S2; Note: References (46-54) are only called out in the SM.

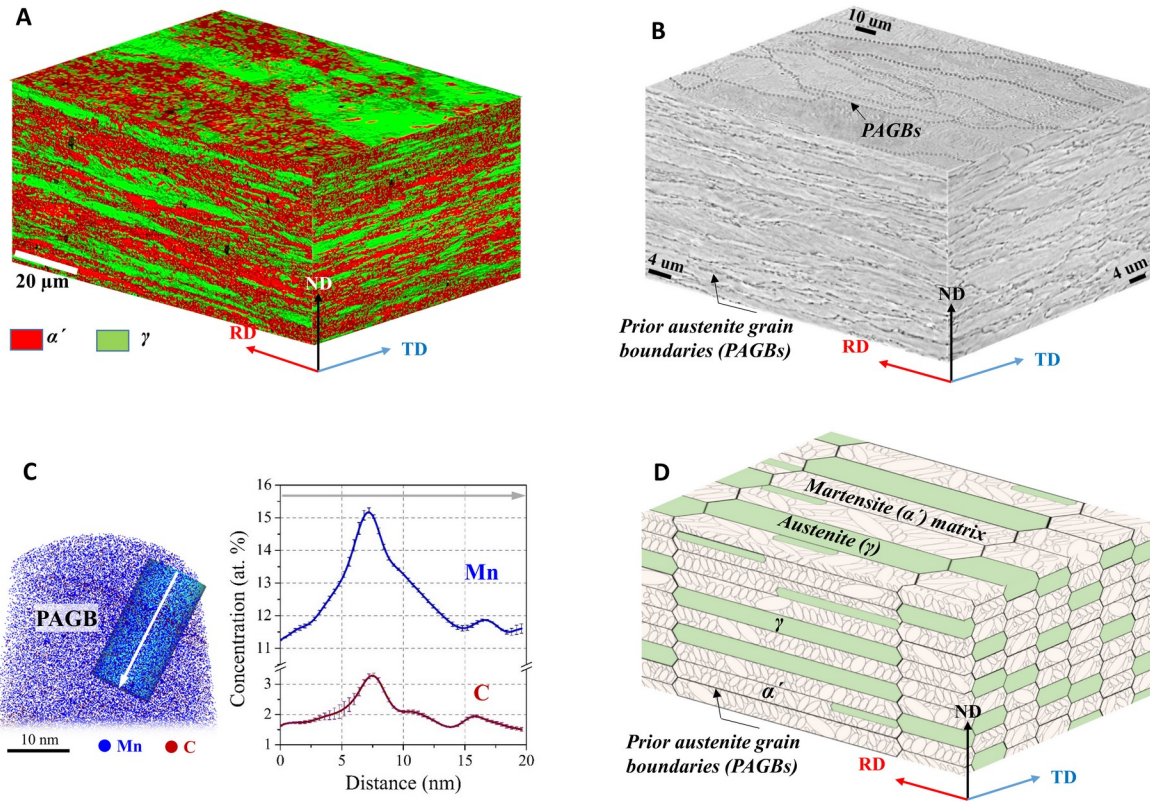


Fig. 1. Microstructure of the present steel. (A) 3-D stereographic microstructure reconstructed by EBSD phase maps scanned on the orthotropic planes perpendicular to the rolling direction (RD), transverse direction (TD), and normal direction (ND), respectively. A heterogeneous laminated duplex microstructure comprising martensitic matrix (α') and elongated austenite (γ) lamellae is exhibited in the present steel. Retained austenite grains are elongated along the RD and slightly stretched along the TD. (B) 3-D stereographic microstructure reconstructed by the prior-austenite grain boundaries (PAGBs) maps imaged by SEM. The PAGBs are marked by the black dotted lines and show a heterogeneous distribution. (C) 3-D ion concentration map, which contains a PAGB and a corresponding 1-D concentration profile across the boundary, shows the segregation of Mn and C to the PAGB. (D) Schematic 3-D model illustrates the microstructural features of the heterogeneous microstructure of the present steel.

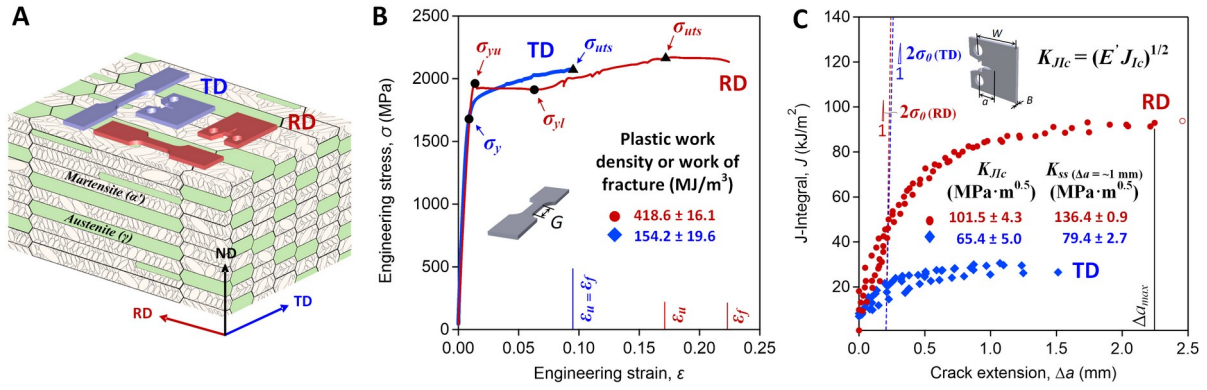
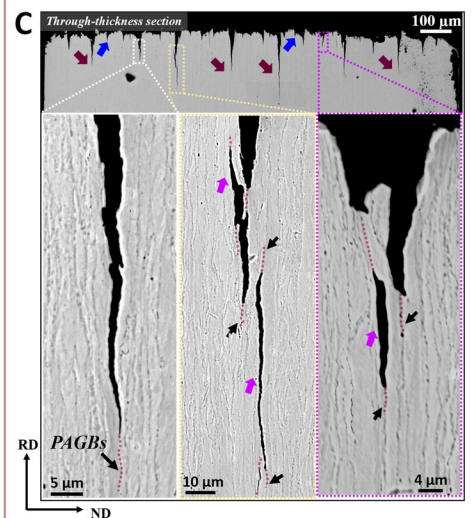
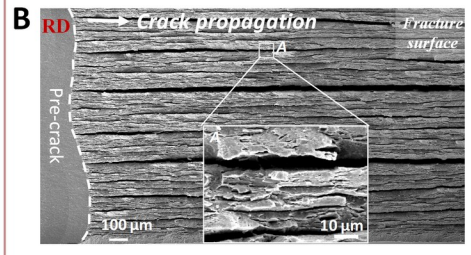
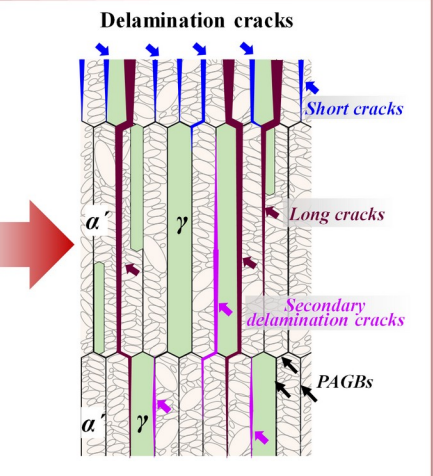
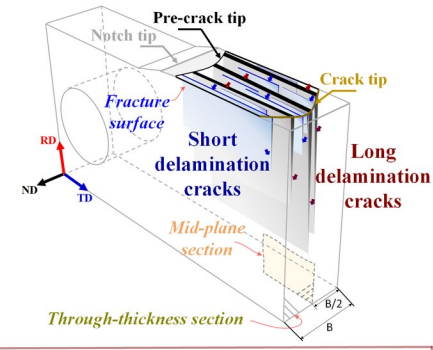


Fig. 2. Tensile and fracture properties of the present steel. (A) Schematic diagram describing the orientations of the dog-bone shaped tensile specimens and the compact-tension C(T) specimens relative to the thin-sheet steel. (B) Engineering stress-strain curves of the present steel deformed under tension along the RD and TD orientations. (C) The J -integral based resistance curves (J -R curves) measured from the C(T) specimens at room temperature.

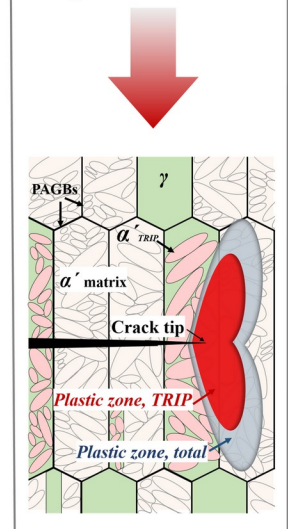
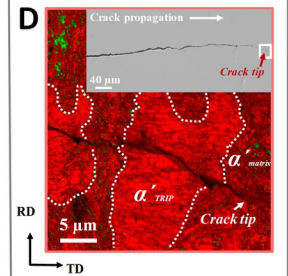
Delamination Toughening



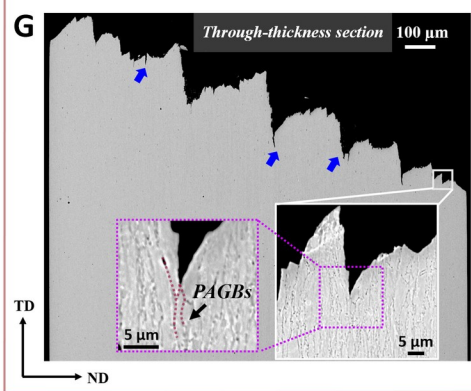
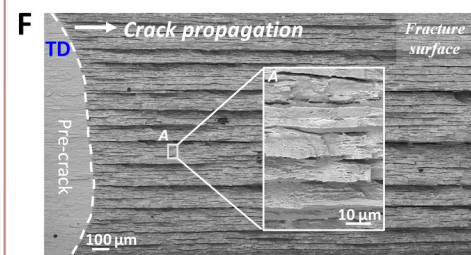
A RD C(T) specimen



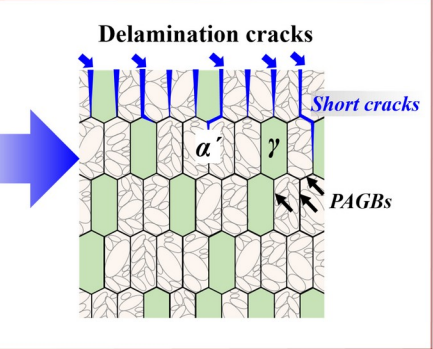
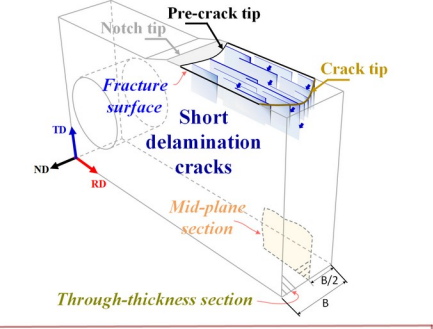
TRIP Toughening



Delamination Toughening



E TD C(T) specimen



TRIP Toughening

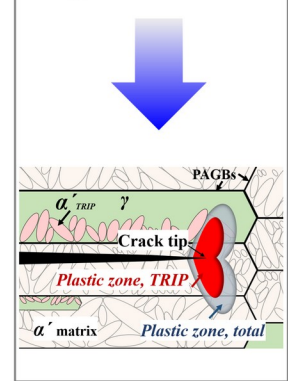
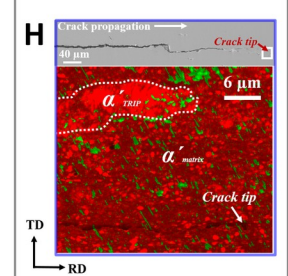


Fig. 3. Toughening mechanisms in the steel. (A, E) The schematic diagrams of the RD and TD C(T) specimens showing the various sections for microstructure characterizations. (B, F) The fracture surfaces of the RD and TD C(T) specimens, clearly showing the thin-layer delamination bands on the fracture surface. (C, G) The SEM images captured on the through-thickness section normal to the fracture surface show the development of delamination cracks along PAGBs. Short delamination cracks (blue arrows) and deeply penetrated ones (red arrows) are found in the RD specimen whereas only shallow-penetrated delamination cracks formed in the TD specimen. Slender cracks disconnected from the fracture surface (pink arrows) were usually observed in the vicinity of the long delamination cracks. Corresponding schematic diagrams reveal that the significantly elongated PAGBs in the RD specimen facilitate the propagation of delamination cracks, while the short PAGBs and numerous PAGBs perpendicular to the crack propagation in the TD specimen hinder the extension of delamination cracks. (D, H) EBSD phase maps overlaid with the image quality maps scanned in the vicinity of the main crack tip on the mid-plane section of C(T) specimens. Schematic diagrams delineating the TRIP-toughening mechanism are shown below. The TRIP-induced martensite (α'_{TRIP}) can be distinguished from the martensite matrix (α'_{matrix}) by higher image quality, due to the fact that the α'_{TRIP} grains transformed from the retained austenite have a lower dislocation density (regions bounded by dashed white lines).

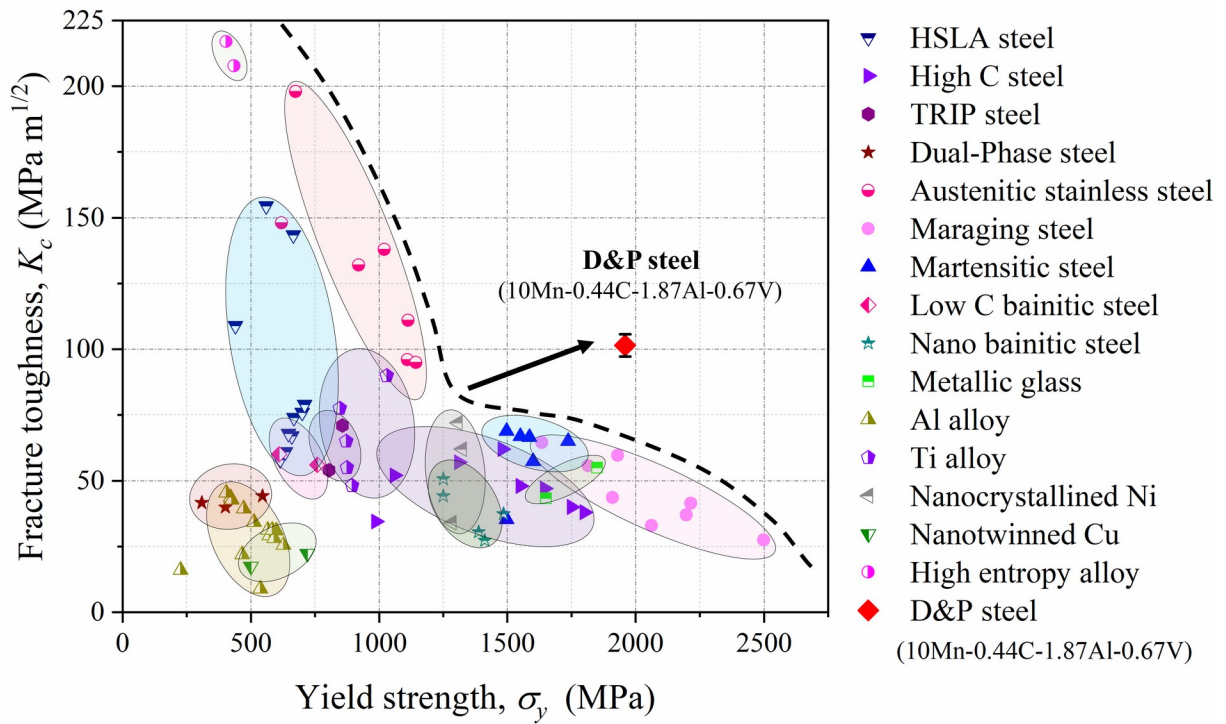


Fig. 4. Ashby map in terms of the fracture toughness versus the yield strength. Our ultrastrong steel overcomes the strength-toughness trade-off shown in most existing structural materials, especially high strength low alloy (HSLA) steels (29, 30), high carbon (C) steels (31), TRIP steels (32), dual-phase steels (33), austenitic stainless steels (34, 35), maraging steels (18, 19, 36), martensitic steels (37, 38), low C bainitic steels (39), nano bainitic steels (40), metallic glass (41), Al alloys (42), Ti alloys (43), nanocrystalline Ni (44), nanotwinned Cu (45), and high-entropy alloys (6, 7). Detailed composition and properties of these compared materials can be found in [Table S2](#).

5

Supplementary Materials for Making Ultrastrong Steel Tough by Grain-Boundary Delamination

L. Liu[†], Qin Yu[†], Z. Wang, Jon Ell, M. X. Huang^{*}, Robert O. Ritchie^{*}.

10

[†]These authors contributed equally to this work.

Correspondence to: mxhuang@hku.hk (M.X.H.); roritchie@lbl.gov (R.O.R.)

15

This PDF file includes:

Materials and Methods

Supplementary Text

Figs. S1 to S9

20

Tables S1 to S2

Materials and Methods

Materials processing

The chemical composition of the material employed in this work was Fe-9.95%Mn-0.44%C-1.87%Al-0.67%V (weight percent). The contents of impurity elements P and S were lower than 50 and 30 ppm, respectively. Thus, the influence of impurities on the mechanical properties was negligible. The steel was produced by a deformed and partitioned treatment (14), the processing details of which are illustrated in Fig. S1 and summarized as follows. The steel was cast in induction melting furnace and then forged into a rectangular ingot with a thickness of 60 mm and a width of 80 mm. The forged ingot was subsequently homogenized at 1150 °C for 2.5 hours and hot rolled to a thickness of 3.8 mm. The hot rolling strip was reheated to 750 °C for 10 min, followed by warm rolling to further elongate the microstructure and introduce more dislocations. The total thickness reduction of warm rolling was 50%. Subsequently, intercritical annealing was performed at 620 °C for 5 hours to facilitate dislocation recovery followed by cold rolling. The cold rolling reduction was about 26%, reducing the final thickness of the steel sheet to 1.4 mm. Finally, the cold rolling strip was partitioned at 300 °C for 6 minutes followed by water quenching to room temperature (RT).

The present steel has an almost fully austenitic microstructure before cold rolling due to the high hardenability, as shown in Fig. S2. No cementite (Fe₃C), which prefers to segregate at grain boundaries and deteriorate toughness, was found in the specimen processed by intercritical annealing due to the addition of Al (14) (Fig. S2). A small fraction of ultrafine ferrite grains was developed during intercritical annealing (Fig. S2). However, the kinetics of ferrite transformation during this annealing was quite slow due to the solute drag effect originating from the high Mn content (46). Numerous prior-austenite grains were transformed into martensite during cold rolling, contributing to the dual-phase microstructure of the present steel (14, 15); however, the prior-austenite grain boundaries (PAGBs) could still be detected in the microstructure after the cold rolling. Partitioning was performed to further increase the mechanical stability of the retained austenite by C diffusion from martensite to austenite. The right shift of the austenite (220) peak after partitioning in the neutron profile, indicating an increase in the lattice parameter of austenite, confirms the C partitioning process (Fig. S4A). The martensite formed during cold rolling was tempered after partitioning, as indicated by comparing the hardness values of the specimens before and after partitioning (Fig. S4B). No fresh martensite was formed during the final cooling stage due to the high hardenability (46). The term “Deformed” refers to the processes of hot rolling, warm rolling, and cold rolling, which generates the highly dislocated duplex lamellar microstructure; the term “Partitioned” refers to the short 300 °C annealing to increase the mechanical stability of the retained austenite.

The segregation of Mn atoms to the austenite grain boundaries can take place during hot rolling (at 900-1150 °C), warm rolling (at 350-750 °C), and subsequent intercritical annealing (at 620 °C for 5 hr). The final partitioning, which was performed at a lower temperature (300 °C) with a short duration (6 mins), had less effect on Mn-segregation due to the sluggish diffusion rate of Mn (47). Therefore, the Mn-enriched austenite grain boundaries formed before cold rolling were retained in the final microstructure, despite the deformation-induced martensitic transformation during cold rolling and subsequent partitioning.

Neutron diffraction characterization

Neutron diffraction characterization was carried out using a deep-penetrating neutron beam with high intensity and good spatial resolution, making it well suited for the structural analysis of complex anisotropic materials (48). Here, the phase fraction of the present steel was estimated by neutron diffraction performed on a General Purpose Powder Diffractometer (GPPD) with a 360°

rotation stage at China Spallation Neutron Source (CSNS). The power of the neutron source was 40 kW. The time-of-flight method was used to collect data over a total scanning time of 6.26 hr. All faces of the sample for neutron diffraction measurement were mechanically polished down to 1 μm , followed by electrical polishing in a solution of 20% perchloric acid and 80% acetic acid (vol.%). The volume fraction of austenite was determined to 47.5% by Rietveld refinement performed on a crystallography data analysis software GSAS-II (49). The measured neutron results and fitted profile are indicated in Fig. S3.

Calculation of dislocation density

The dislocation density of the present steel was calculated using a combination of the modified Williamson-Hall (MWH) and modified Warren-Averbach (MWA) method (50, 51) based on the neutron diffraction profile (Fig. S3). According to the MWH method, the full width at half maximum (FWHM), ΔP , of the diffraction peaks is a function of the average crystallite size (D) and the dislocation density (ρ) as follows (51):

$$\Delta P = 0.9 / D + \pi A^2 b^2 \rho^{1/2} (P^2 \bar{C}) / 2 + O(P^4 \bar{C}^2) \quad (1)$$

where b and P represent the magnitude of the Burgers vector and the exact Bragg position, respectively. A is a constant depending on the effective outer cutoff radius of dislocations R_e . O represents the high order terms in $P^2 \bar{C}$ and is neglected for calculation. \bar{C} is the average contrast factor. For each $\{hkl\}$ reflection, \bar{C} can be determined by (52):

$$\bar{C} = \bar{C}_{h00} \left[1 - q \left[(h^2 k^2 + k^2 l^2 + l^2 h^2) / (h^2 + k^2 + l^2) \right] \right] \quad (2)$$

where \bar{C}_{h00} is a constant depending on the anisotropic elastic constants C_{11} , C_{12} and C_{44} . q is a variable determined by the fraction of screw and edge dislocations. P and ΔP can be directly obtained from the neutron profile. Therefore, the values of D , $A^2 \rho^{1/2}$ and q can be determined by the best linear fitting between ΔP and $P^2 \bar{C}$ (Fig. S6A). According to the MWA method, R_e and ρ can be estimated by Fourier analysis as (53):

$$\ln A(L) \cong \ln A^s(L) + Y(L)(P^2 \bar{C}) + O'(P^4 \bar{C}^2) \quad (3)$$

$$Y(L) = -(\rho \pi b^2 L^2 / 2) \ln(R_e / L) \quad (4)$$

where L , $A(L)$, $A^s(L)$ and O' represents the Fourier length, the real part of the Fourier coefficient for the intensity distribution of the diffraction profile, the size contribution and higher-order terms of $P^2 \bar{C}$, respectively. Eq. (4) can be rewritten as:

$$Y(L) / L^2 = (\rho \pi b^2 / 2) \ln L - (\rho \pi b^2 / 2) \ln R_e \quad (5)$$

With the value of \bar{C} determined before, the values of $Y(L)$ for various L were obtained by fitting $\ln A(L)$ against $P^2 \bar{C}$ according to Eq. 3, as shown in Fig. S6B. The dislocation density can be subsequently determined by linear regression on the linear part of $Y(L) / L^2$ and $\ln L$ data according to Eq. 5 (53).

Transmission electron microscopy characterization

Transmission electron microscopy (TEM) was carried out to characterize the dislocation substructure of our steel, as indicated in Fig. S5. TEM observations were performed in an FEI Tecnai G2 20 TEM operated at 200 kV. The samples for TEM characterization were prepared by mechanical polishing down to a thickness of 100 μm , followed by twin-jet electro-polishing in a solution of 5% perchloric acid, 30% glycerinum and 65% ethanol (vol. %) performed at -10 $^{\circ}\text{C}$ with a potential of 36 V.

Atom probe tomography characterization

The 3D atom probe tomography (APT) measurements were performed to characterize the segregation of Mn from grain interior to PAGBs. The APT measurements were performed in a LEAP 5000XR instrument working in voltage mode at a temperature of about 50 K, a pulse repetition rate of 200 kHz, a pulse fraction of 20%, and an evaporation detection rate of 0.2% atom per pulse. 3D reconstructions were carried out by Imago Visualization and Analysis Software (IVAS) version 3.8. The needle-shaped specimens for APT characterization were fabricated from the plane perpendicular to the normal direction of the present steel by lift-out method (54) and annular milling performed in an FEI Scios focused ion beam/scanning electron microscope (FIB/SEM). Before FIB milling, the sample was vibration-polished and etched to reveal PAGBs.

Mechanical characterization

In order to characterize the uniaxial tensile properties, dog-bone shaped rectangular specimens with a gauge cross-section of 4.0 mm \times 1.4 mm and a gauge length of 10 mm were fabricated from the present steel thin sheet using wire electrical discharge machining (EDM). As illustrated in Fig. 2A, the loading direction for the RD (or TD) tensile specimens was aligned along (or perpendicular to) the elongated austenitic grains. Before the tensile testing, the surfaces of the flat specimens were ground using 1200 grit SiC paper. A strain-gauged extensometer Model 3442 (Epsilon, Jackson, WY, USA) was utilized to measure the engineering strain within the gauge section. Tensile tests were performed at room temperature with a 50 kN electro-servo hydraulic load frame at an engineering strain rate of $1.0 \times 10^{-3} \text{ s}^{-1}$. Three tensile specimens were tested in each orientation.

Tensile properties including the yield strength¹, σ_y , ultimate tensile strength, σ_{uts} , uniform elongation, ε_u and elongation to fracture, ε_f , were determined from the tensile engineering stress-strain curves; their average values and the standard deviations are summarized in Table S1. True stress-strain curves were also calculated in order to extract the plastic work density (*i.e.*, the work

of fracture), $u_f = \int^{\varepsilon_{f,p}} \sigma d\varepsilon_p$, during tensile fracture; this was determined from the area under the true stress-plastic strain curve, where $\varepsilon_{f,p}$ is the plastic strain corresponding to the elongation to failure, ε_f .

¹ Since the initial plastic deformation in the RD tensile specimens was dominated by the Lüders band propagation, both the upper yield strength, σ_{us} , and the lower yield strength, σ_{ls} , were characterized. For the TD specimens, where a continuous elastic-plastic yielding was exhibited, we determined the yield strength following the engineering 0.2% offset approach.

For the evaluation of the fracture toughness, in accordance with ASTM Standard E1820 (17), compact-tension C(T) specimens, with a thickness of $B = 1.4$ mm and width of $W = 18$ mm, were cut from the present steel thin sheet using wire EDM. Two specimen orientations were prepared, *i.e.*, the RD and TD specimens, where the notch (or crack propagation) direction is perpendicular and parallel to the longitudinal direction of the austenitic grains, respectively (Fig. 2A). Notches, 1.4 mm in depth with a root radius of ~ 100 μm , were cut in all C(T) specimens using wire EDM. Before testing, all specimen surfaces were ground and polished to 1- μm mirror finish to enable the measurement of crack length using Questar QM100 long-distance optical microscope. Prior to the fracture toughness measurement, all the C(T) specimens were fatigue pre-cracked to a crack length with a/W ratio of ~ 0.5 using a 5 kN servo-hydraulic MTS 831 load frame (MTS Corporation, Eden Prairie, MN, USA). Fatigue pre-cracking was performed under load control at a stress-intensity range $\Delta K = K_{max} - K_{min}$ of 10-15 $\text{MPa}\cdot\text{m}^{1/2}$ at 10 Hz frequency with a load ratio P_{min}/P_{max} of 0.1.

Nonlinear elastic-fracture mechanics was used evaluate the fracture toughness of the present steel; specifically, the crack-resistance behavior (R-curve) was characterized in terms of the J -integral as a function of crack growth, where J is the rate of change in potential energy per unit increase in crack area for a nonlinear-elastic solid. C(T) specimens were loaded under displacement control at a constant displacement rate of 0.1 mm/min. The onset of cracking and the subsequent subcritical crack growth were directly measured by a long-distance optical microscope, as well as determined using the unloading compliance method in accordance with the ASTM Standard E1820 (17). During tensile loading, the C(T) specimen was periodically unloaded to $\sim 20\%$ of the peak load to record elastic unloading compliance by using an Epsilon clip-on gauge mounted in the load-line of the specimens. The crack length, a_i was calculated from the elastic unloading compliance using the compliance expression of the C(T) specimen:

$$a_i / W = 1.000196 - 4.06319u + 11.242u^2 - 106.043u^3 + 464.335u^4 - 650.677u^5, \quad (6)$$

$$u = \frac{1}{(BEC_{c(i)})^{1/2} + 1}, \quad (7)$$

where B is the specimen thickness and $C_{c(i)}$ is the rotation-corrected elastic unloading compliance. For each crack length a_i , the J_i -integral was calculated as the sum of the elastic $J_{el(i)}$ and plastic $J_{pl(i)}$ components:

$$J_i = J_{el(i)} + J_{pl(i)} = K_i^2 / E' + J_{pl(i)}, \quad (8)$$

where $E' = E$ (Young's modulus) in plane stress or $E/(1 - \nu^2)$ in plane strain (ν is Poisson's ratio). For the present steel, E and ν are 200 GPa and 0.3, respectively. The linear elastic stress intensity K_i was defined for C(T) specimen from (17):

$$K_i = \frac{P_i}{(BB_N W)^{1/2}} f\left(\frac{a_i}{W}\right), \quad (9)$$

$$f\left(\frac{a_i}{W}\right) = \frac{(2 + \frac{a_i}{W})[0.886 + 4.64(\frac{a_i}{W}) - 13.32(\frac{a_i}{W})^2 + 14.72(\frac{a_i}{W})^3 - 5.6(\frac{a_i}{W})^4]}{(1 - \frac{a_i}{W})^{3/2}}, \quad (10)$$

where P_i is the applied load prior to the partial unloading, B and B_N are the specimen thickness and the net side-grooved thickness, respectively. The crack-growth corrected plastic component of $J_{pl(i)}$ was evaluated from the following equations (17):

$$J_{pl(i)} = \left[J_{pl(i-1)} + \left(\frac{\eta_{pl(i-1)}}{b_{(i-1)}} \right) \frac{A_{pl(i)} - A_{pl(i-1)}}{B_N} \right] \left[1 - \gamma_{(i-1)} \frac{a_{(i)} - a_{(i-1)}}{b_{(i-1)}} \right] \quad (11)$$

where $\eta_{pl(i-1)} = 2 + 0.522 \frac{b_{(i-1)}}{W}$ and $\gamma_{(i-1)} = 1 + 0.76 \frac{b_{(i-1)}}{W}$. $A_{pl(i)}$ is the plastic area under the force vs. the load-line displacement curve, and $b_i = W - a_i$ is the ligament length. Using Eqs. (6) to (11), we can construct the J - Δa resistance curve by calculating the J_r -integral corresponding to the crack extension Δa_i as the difference of the crack length a_i and the initial crack length a_0 including the notch length and the pre-crack length.

The provisional toughness J_Q was determined as the intersection of the R-curve and the 0.2 mm offset/blunting line with a slope of $2\sigma_0$, where $\sigma_0 = 0.5(\sigma_y + \sigma_{us})$ is the flow stress (now referred to as the effective yield strength in the ASTM Standard 1820) as the average value of the yield strength² and the ultimate tensile strength. According to the ASTM Standard 1820, for the provisional toughness J_Q to be considered as a size-independent fracture toughness (J_{Ic}), the validity requirements for the J -field dominance and plane-strain conditions must be respectively met, i.e., that $b_0, B > 10J_Q/\sigma_0$, where the b_0 and B are the initial ligament length and the specimen thickness, respectively. The corresponding K -based fracture toughness values were then computed using the standard mode-I J - K equivalence relationship, $K_{Jic} = (E'J_{Ic})^{1/2}$. The flow, or effective yield, stress is 2063.5 MPa and 1879.5 MPa for the RD and TD specimens, respectively. Accordingly, the calculated $10J_Q/\sigma_0$ values for the RD and TD specimens were 0.23 mm and 0.10 mm, respectively. The J_Q and K_Q of both RD and TD specimens (Table S1) thus satisfy the specimen size requirements ($b_0, B > 10J_Q/\sigma_0$) for both J -field dominance and plane-strain conditions, and therefore can be regarded as ASTM valid J_{Ic} and K_{Jic} toughness values. A provisional crack-growth fracture toughness (K_{SS}) was calculated from the crack-growth J -integral (J_{SS}) evaluated from the J - Δa resistance curve at $\Delta a = \sim 1$ mm (Table S1). To assess the ASTM validity of the K_{SS} and J_{SS} , the $10J_{SS}/\sigma_0$ values for the RD and TD specimens were checked to be 0.41 mm and 0.15 mm, respectively. Both values meet the ASTM specimen size requirements for J -field dominance and plane-strain conditions. Thus, the crack-growth toughness K_{SS} and J_{SS} are ASTM valid as well.

² For the RD C(T) specimen, the upper yield strength, σ_{yu} is used to calculate the flow stress.

Fractographic characterization

Fractography examinations were performed on featured regions along the crack propagation direction on the separated fracture surfaces as well as on the planes perpendicular to the fracture surface using a Hitachi S-4300SE/N SEM (Hitachi America, Pleasanton, CA, USA) operating in the secondary electron (SE) imaging mode at 5-15 kV.

To specifically examine the crack-path profile and discern the deformation mechanisms in the vicinity of the crack tip and wake under plane-strain conditions, some C(T) specimens were interrupted during the fracture toughness testing and sliced through the thickness into two halves at the mid-section thickness. The interior surface of one half was progressively ground and polished to a 0.05- μm surface finish followed by a final vibration polishing using 0.05- μm colloidal silica. The microstructure along the crack wake and the crack-tip region were imaged using back-scattered electrons (BSE) in the Hitachi S-4300SE/N SEM operating at 20 kV. To further clarify the deformation modes, electron back-scatter diffraction (EBSD) scans were performed in the vicinity of the crack tip and wake using the FEI Strata DB235 SEM operated at 20 kV using a TEAMTM EBSD analysis system (Ametek EDAX, Mahwah, NJ, USA) with a step size of 80 nm. To reveal the morphologies of prior-austenite grain boundaries (PAGBs), vibration polished samples were further etched for 8 to 11 mins at ambient temperature in a saturated aqueous solution of picric acid containing 2 mls of “teepol” (sodium alkyl sulfonate acting as the “wetting” agent).

The microstructure of the intercritical annealed strip was characterized by EBSD (Symmetry EBSD detector, Oxford Instrument, UK) analysis performed on a Zeiss Sigma 300 FEG SEM operated in 20 kV with a step size of 30 nm. The samples for EBSD scanning were prepared by electro-polishing, as described in Section 1.2.

Hardness test

The hardness of the deformed as well as the deformed & partitioned (D&P) specimens was measured by a Mitutoyo AVK-C2 Vickers hardness testing machine. An indentation load of 5 g was applied. The diameter of the indents was about 110 μm and the separation between any two neighboring indentations was at least 300 μm . The martensitic matrix was tempered after partitioning at 300 °C, as revealed by the decrease of hardness after partitioning (Fig. S4B).

Supplementary Text

Statistical analysis of delamination cracks

To confirm the occurrence of delaminations and analyze the length distribution of delamination cracks, various samples were cut from the C(T) specimens for microstructure characterization. These specimens were first loaded and then partially unloaded according to the ASTM Standard E1820 for toughness measurement. After the crack propagated to a certain distance, C(T) specimen was broken into two parts, which were marked as Part A and Part B. Each part was sliced along the through-thickness section (perpendicular to the fracture surface) at locations with different distances to the crack tip. Subsequently, the through-thickness sections of these samples were mechanically and vibration polished for SEM imaging. The lengths of delamination cracks were measured and statistically analyzed. Results are summarized in Figs.

[S7](#) and [S8](#). Two categories of delamination cracks with lengths shorter than 50 μm and longer than 50 μm were observed in the RD specimen ([Fig. S7](#)). However, only limited amount of delamination cracks shorter than $\sim 50 \mu\text{m}$ were present in the TD specimen, no matter how far the main crack propagated ([Fig. S8](#)).

5

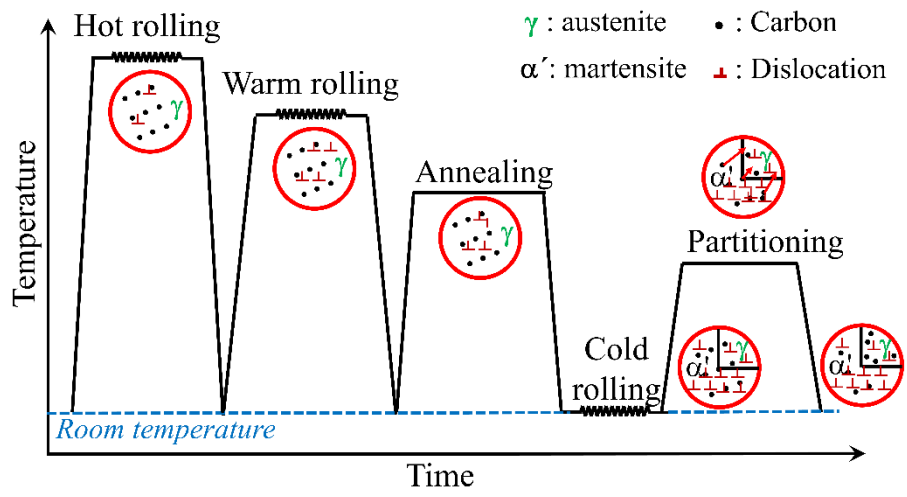


Fig. S1.

Schematic illustration of the thermomechanical process used to produce the steel in this work.

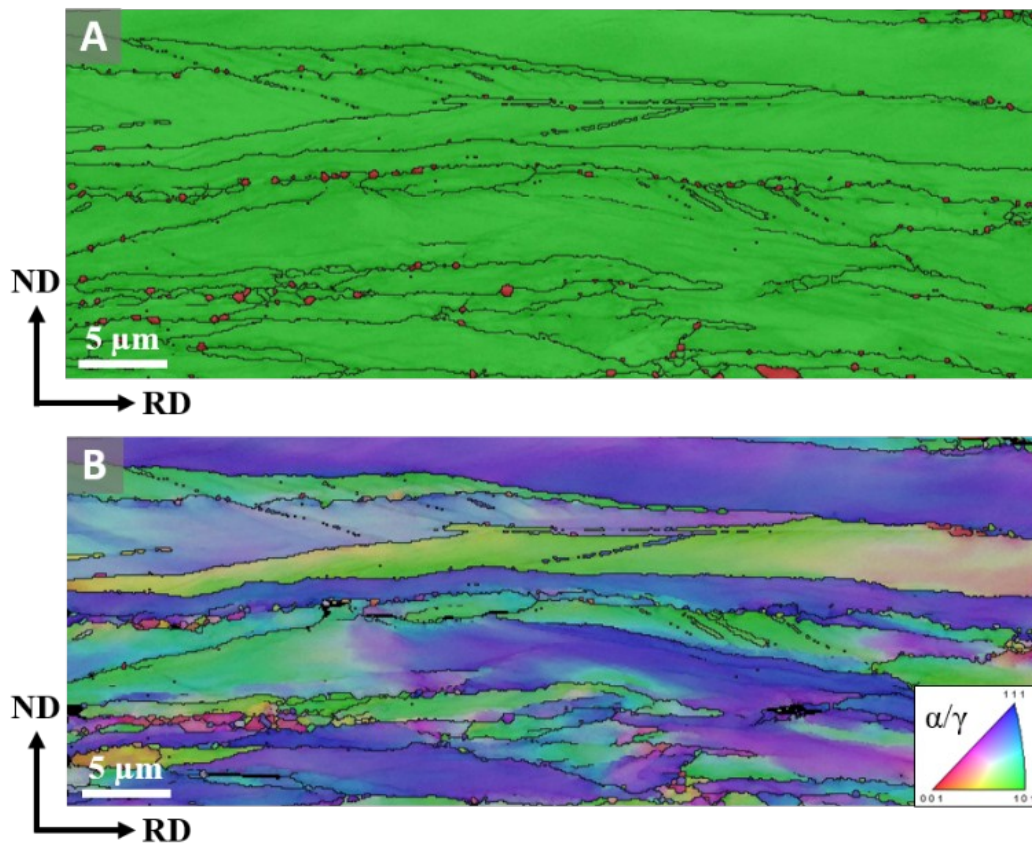


Fig. S2.

Microstructure of the intercritical annealed specimen. (A) EBSD phase map. Green: austenite; Red: ferrite. (B) EBSD orientation map. High-angle grain boundaries ($>15^\circ$) are marked by black lines.

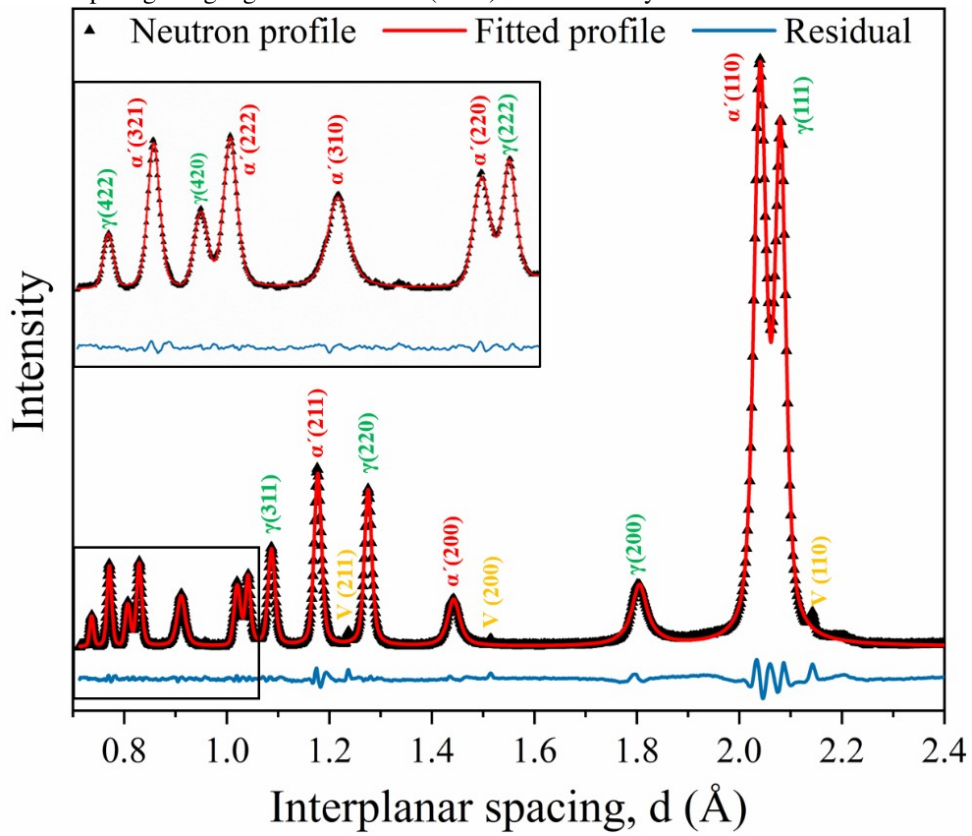


Fig. S3.

Neutron diffraction spectrum of the present steel measured with the powder diffractometer at the China Spallation Neutron Source (CSNS). The interplanar d -spacing is the distance between successive, parallel $\{hkl\}$ planes. Peaks of vanadium were detected as a vanadium container was used to hold samples during the neutron diffraction measurement.

5

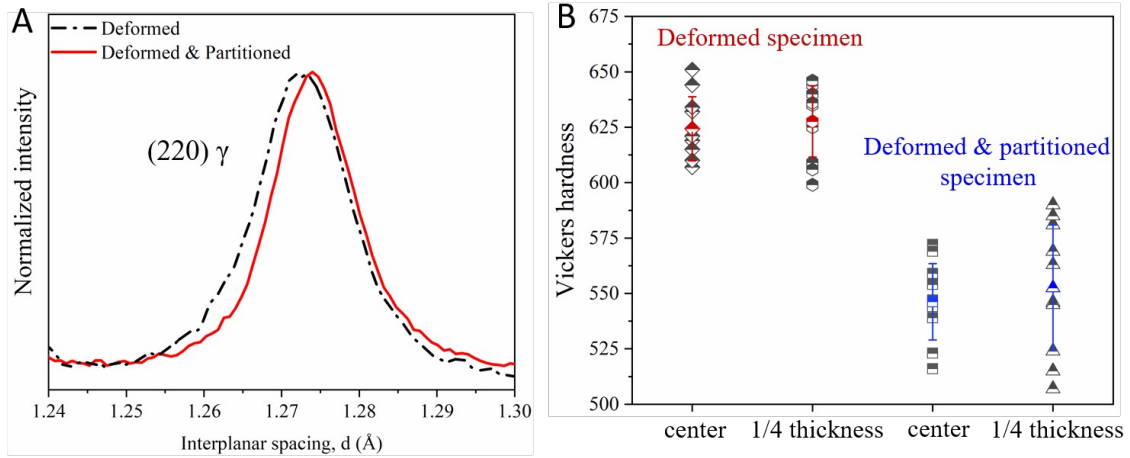


Fig. S4.

(A) The neutron profiles of the deformed as well as the deformed and partitioned (D&P) specimens. (B) The Vickers hardness values of the deformed and D&P specimens measured at locations in the 1/2 (center) or 1/4 thickness to the surface.

5

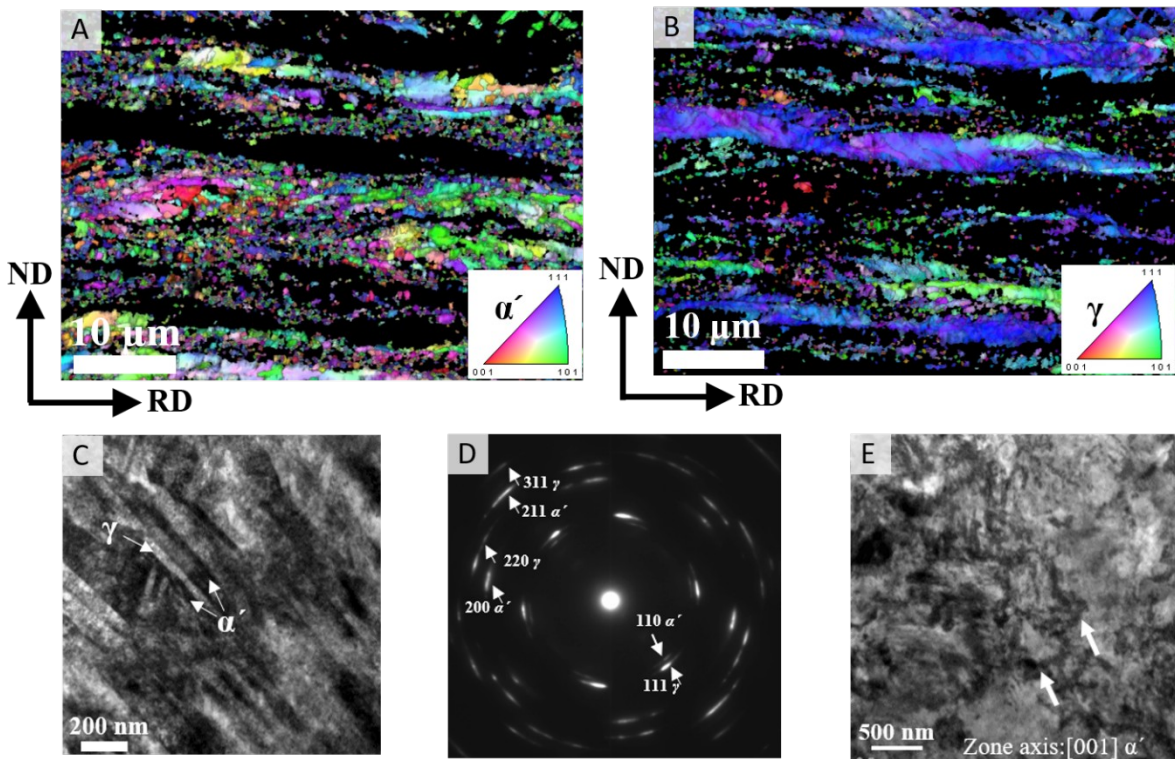


Fig. S5.

The EBSD orientations maps of (A) martensite and (B) austenite scanned on the plane normal to TD orientation showing that nano-sized grains dominate the martensitic matrix. (C) TEM bright field image reveals that ultrafine austenite lamellas embedded in martensite lathes, as confirmed by (D) the select area diffraction pattern (SADP). (E) Dislocation cell structure in the martensitic matrix captured by TEM.

5

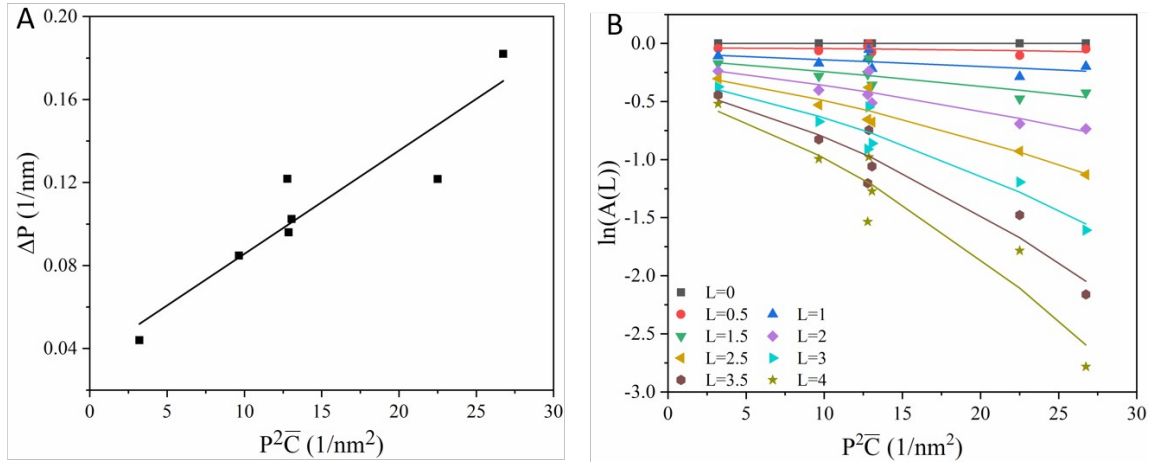


Fig. S6.

(A) Modified Williamson-Hall (MWH) plot and (B) modified Warren-Averbach (MWA) plot obtained from the martensite peaks in the neutron profile of the present steel.

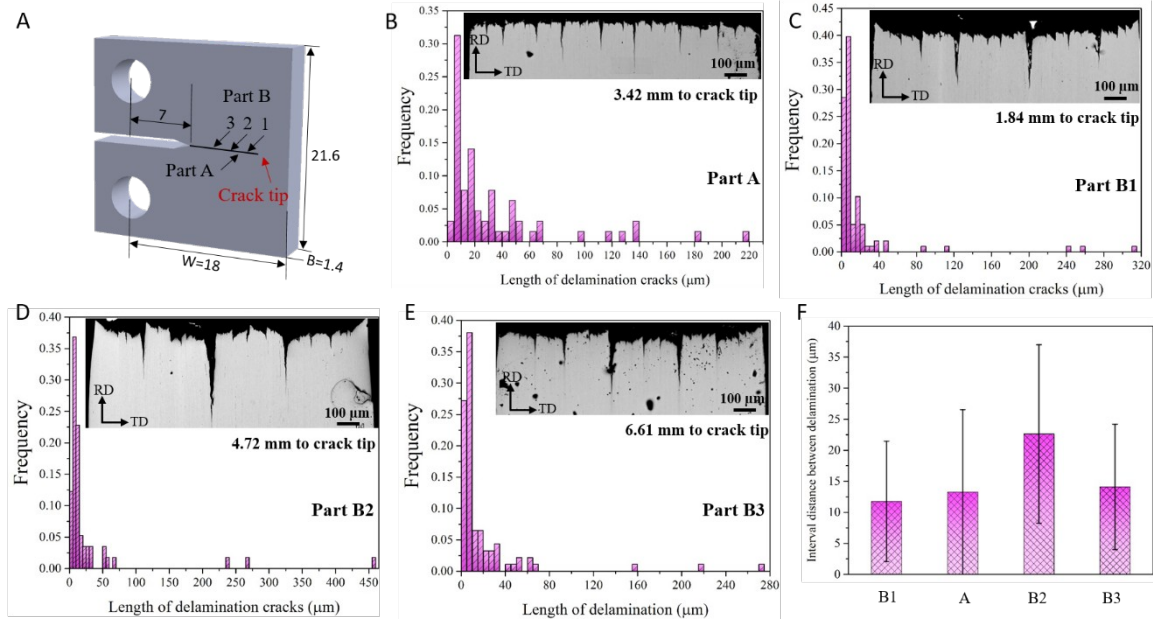


Fig. S7.

(A) Schematic illustration showing the position of samples cut from an RD C(T) specimen for microstructure characterization. The unit of sample geometries is millimeter (mm). (B-E) SEM images obtained at a section normal to fracture surface showing the distribution of delamination cracks and the corresponding statistical analysis of the length of delamination cracks in the RD specimens. (F) The average interval length between the delamination cracks was estimated from the SEM images shown in B-E.

5

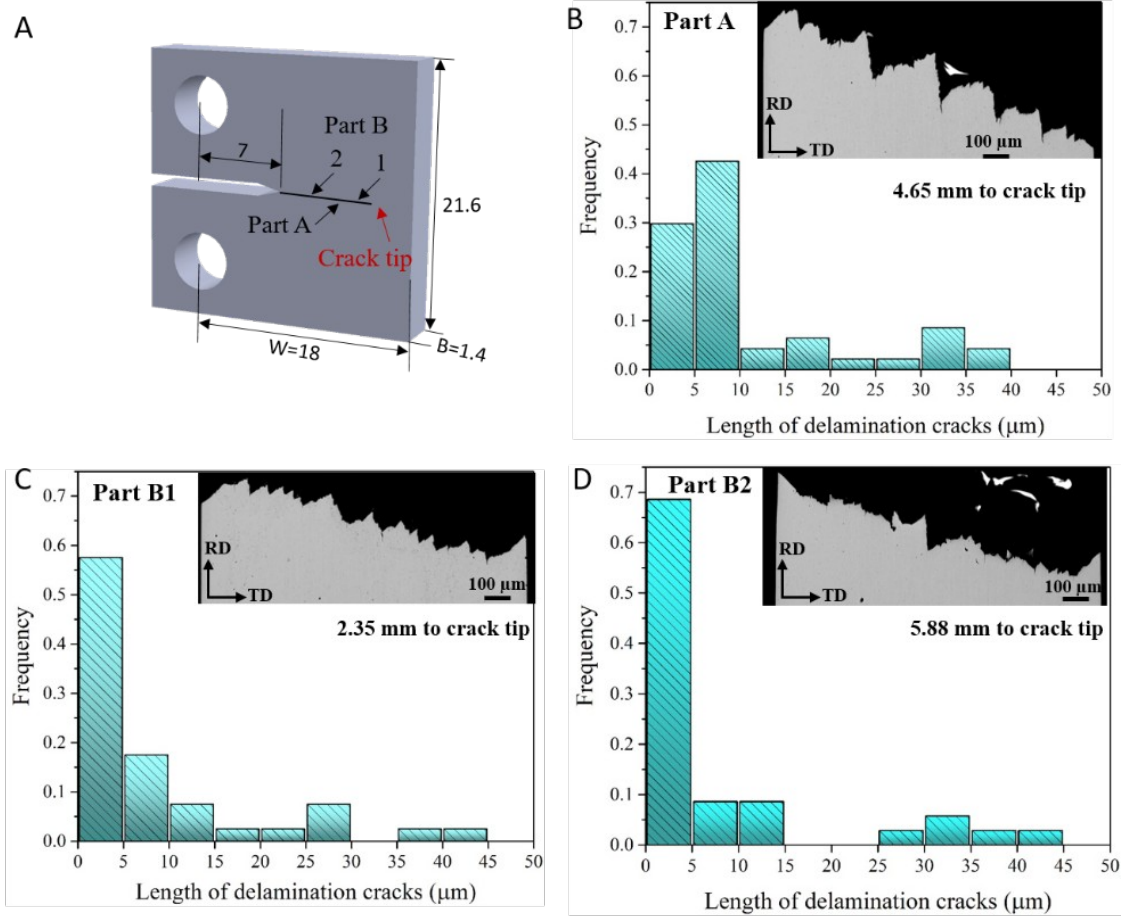


Fig. S8.

(A) Schematic illustration showing the position of samples cut from a TD C(T) specimen for microstructure characterization. The unit of sample geometries is millimeter (mm). (B-D) SEM images obtained at the section normal to fracture surface showing the distribution of delamination cracks and the corresponding statistical analysis of the length of delamination cracks in the TD specimen.

5

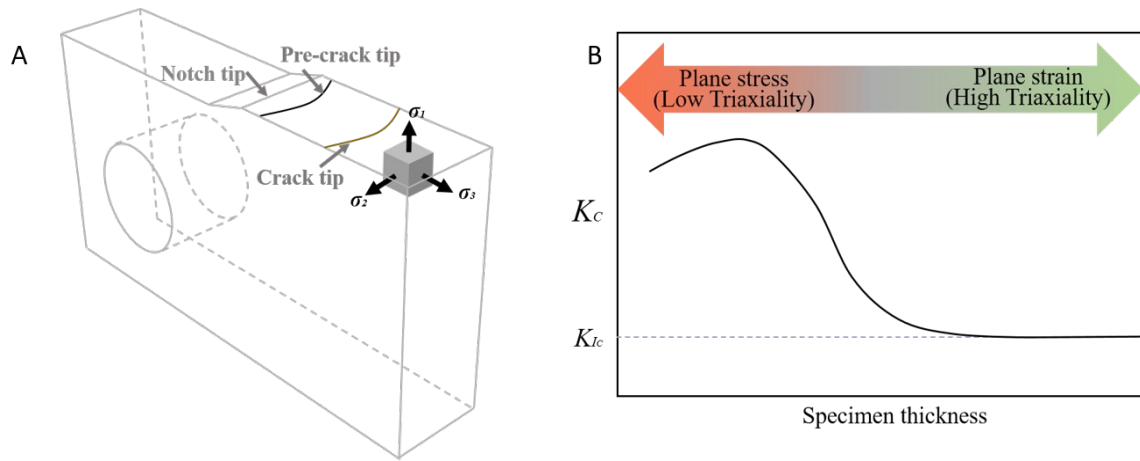


Fig. S9.

(A) The schematic diagram of the C(T) specimen showing that a triaxial tensile stress state exists ahead of a crack tip under plane-strain conditions. (B) Schematic diagram illustrating the variation of the measured toughness with respect to specimen thickness.

5

Table S1. Uniaxial tensile and fracture toughness properties of the present steel at room temperature.

Property	RD	TD
0.2%-offset yield strength, σ_y (MPa)	-	1714 \pm 5
Upper yield strength, σ_{yu} (MPa)	1978 \pm 16	-
Lower yield strength, σ_{yl} (MPa)	1916 \pm 4	-
Ultimate tensile strength, σ_{uts} (MPa)	2144 \pm 27	2048 \pm 35
Uniform elongation, ε_u (%)	19.0 \pm 1.2	8.3 \pm 1.6
Elongation to failure, ε_f (%)	21.6 \pm 0.8	8.3 \pm 1.6
Plastic work density (or work of fracture), u_f (MJ·m ⁻³)	418.6 \pm 16.1	154.2 \pm 19.6
J -integral at crack initiation, J_{Ic} (kJ·m ⁻²)	46.9 \pm 4.0	19.6 \pm 2.9
Fracture toughness at crack initiation, K_{Jic} (MPa·m ^{1/2})	101.5 \pm 4.3	65.4 \pm 5.0
Crack growth J -integral at $\Delta a = \sim 1$ mm, J_{SS} (kJ·m ⁻²)	84.6 \pm 1.1	28.7 \pm 1.90
Crack growth toughness at $\Delta a = \sim 1$ mm, K_{SS} (MPa·m ^{1/2})	136.4 \pm 0.9	79.4 \pm 2.7

Table S2. Composition and properties of the materials compared in the Ashby map (Fig. 4).

Material	Composition (wt.%)	σ_y (MPa)	K_c (MPa·m^{1/2})	Ref.
HSLA steels	Fe/0.35C/1.5Mn/0.5Si/0.025Al/0.02Ti/0-0.1V	440-666	68-154.5	29
	Fe/0.14C/1.56Mn/0.5Si/0.042Cr/0.114Mo	615-710	58-79	30
High C steels	Fe/1.02C/0.4Mn/2.45Si/0.2Ni	988-1800	34.5-62	31
TRIP steels	Fe/0.21C/1.5Mn/1.49Si/1Cr	805-857	54-71	32
Dual-phase steels	Fe/0.097C/0.49Mn/0.06Si	309-545	40-41.6	33
Austenitic stainless steels	Fe/16.5Cr/0.02C/0.37Si/1.42Mn	920-1144	95-138	34
	Fe/16Ni/14.3Cr/0.2Ti/2.4Mo/1.6Mn/0.54Si	620-675	148-198	35
Maraging steels	Fe/18Ni/7-8.5Co/1/0.3-0.5Ti/4.6-5.2Mo	2197-2215	37-41.4	18
	Fe/18-19Ni/11.5-12.5Co/1.3-1.6Ti/4.6-5.2Mo	2061.61	30	18
	Fe/18Ni/15Co/1.1Ti/7Mo	1654.8	51.9	19
	Fe/18.26Ni/8.8Co/4.8Mo/0.66Ti	1815-1930	43.6-59.7	36
Martensitic steels	Fe/0.4C/0.8Mn/1.6Si/0.76Cr/0.4Mo/1.76Ni	1497-1737	35.3-68.9	37
	Fe/0.4C/0.8Mn/0.24Si/0.72Cr/0.24Mo/1.65Ni/0.2Cu	1551-1600	57.4-66.9	38
Low C bainitic steels	Fe/0.37C/0.7Mn/0.88Si/1Cr/0.79Mo/0.14V	610-759	56-60	39
Nano bainitic steels	Fe/0.8C/1.6Si/2Mn/0.14Mo/1Cr/1.5Co/0-1Al	1250-1485	27-51	40
Metallic glass	Pd79/Ag3.5/P6/Si9.5/Ge2 (at. %)	1650-1850	43.3-55	41
Al alloys	Al/5.7-8.7Zn/1.8-2.7Mg/1.4-2.3Cu	226-627	9-45.4	42
Ti alloys	Ti/6Al/4V	825-869	65-90	43
	Ti/5Al/2.5Fe	895	39.2-57.1	43
	Ti/5Al/1.5B	820-930	55	43
	Ti/13Nb/13Zr	836-908	65	43
	Ti/12Mo/6Zr/2Fe	1000-1060	88-92	43
Nanocrystalline Ni	Pure nanocrystalline nickel	1283-1324	34-72	44
Nanotwinned Cu	High-purity copper	500-720	17.5-22.3	45
High/medium entropy alloys	CrMnFeCoNi	404	217	6
	CrCoNi	435	207.7	7
Present steel	Fe/10Mn/0.44C/1.87Al/0.67V	1978±16	101.5±4.3	/